AIAA JOURNAL
Vol. 41, No. 11, November 2003

Implicit Technique for Three-Dimensional Turbulent Magnetoaerodynamics

Datta V. Gaitonde* and J. Poggie†
U.S. Air Force Research Laboratory, Wright–Patterson Air-Force Base, Ohio 45433

A high-resolution numerical procedure designed to simulate three-dimensional nonideal magnetogasdynamic (MGD) phenomena on complex configurations is extended to enhance computational efficiency and physical fidelity. A loosely coupled approximately factored implicit method is developed to overcome time-step size limitations of explicit methods. A sub-iteration strategy is included to recover up to second-order time accuracy. Verification exercises, covering wave propagation and diffusion phenomena, are presented to demonstrate accuracy and characterize the efficiency of the numerical procedure. Because the aerodynamic environment will exhibit relatively small electrical conductivities and large compensatory magnetic fields, a low magnetic Reynolds number Re_σ formulation and its solution procedure are described and verified by considering MGD-control of a compressible, laminar flat-plate boundary layer at different interaction parameters. A two-equation k-ϵ turbulence model with low-Reynolds-number near-wall terms is incorporated with additional expressions to reproduce the damping effect of the magnetic field. The effect of a magnetic dipole on a supersonic turbulent flat-plate boundary layer is examined. An exploratory study of MGD control of flow past a classic reentry vehicle configuration demonstrates the capabilities of the numerical scheme.

Nomenclature

A, B, C	=	inviscid flux Jacobians
a, b	=	coefficient in compact differencing
$\boldsymbol{B}$	=	magnetic field vector
C_p	=	specific heat at constant pressure
$C_\mu, C_\epsilon 1, C_1^M$	=	closure coefficients in turbulence model
$\boldsymbol{E}$	=	electric field vector
e	=	total energy without magnetic field component
$\boldsymbol{F}, \boldsymbol{G}, \boldsymbol{H}$	=	flux vectors
J	=	mesh Jacobian
$\boldsymbol{j}$	=	current vector
k	=	thermal conductivity; turbulent kinetic energy
M	=	Mach number
P	=	static plus magnetic pressure
P_k	=	production term in k equation
Pr	=	Prandtl number
Pr_t	=	turbulent Prandtl number
p	=	static pressure
Q	=	viscous flux Jacobians
Q	=	magnetic interaction parameter
Q_{ht}	=	heat flux term
R	=	residual
R_b	=	magnetic pressure number
Re	=	Reynolds number
Re_σ	=	magnetic Reynolds number
$\boldsymbol{S}$	=	source term vector
T	=	temperature
t	=	time
$\boldsymbol{U}$	=	velocity vector
u, v, w	=	Cartesian velocity components
$\boldsymbol{X}$	=	conserved vector
x, y, z	=	Cartesian coordinates
Z	=	total conserved energy
Γ	=	coefficient in compact differencing
γ	=	ratio of specific heats
Δ	=	difference operator
δ	=	boundary-layer thickness
ϵ	=	turbulence energy dissipation rate
μ_m	=	magnetic permeability
μ_t	=	eddy viscosity coefficient
ξ, η, ζ	=	curvilinear coordinates
ρ	=	density
σ	=	electrical conductivity
$\sigma_k, \sigma_\epsilon$	=	closure coefficients in turbulence model
$\bar{\bar{\tau}}$	=	shear stress tensor
ϕ	=	electrical potential; time-integration parameter

Subscripts

f	=	fluid dynamic components
m	=	magnetic field components
ref	=	reference

Superscript

p	=	subiteration counter

Received 22 June 2002; revision received 15 May 2003; accepted for publication 15 May 2003.

*Technical Area Leader, Computational Sciences Branch, Aeronautical Sciences Division, Air Vehicles Directorate. Associate Fellow AIAA.

†Research Engineer, Computational Sciences Branch, Aeronautical Sciences Division, Air Vehicles Directorate. Senior Member AIAA.

I. Introduction

THE possibility of using electromagnetic interactions to exert control on hypersonic flowfields is receiving renewed attention in the quest for sustained hypersonic flight and easier access to space. These techniques exploit the natural or artificially enhanced electrical conductivity of the high-speed environment and show the potential to be far more effective than conventional methods at alleviating severe thermal and drag loads, as well as inefficiencies that presently preclude the use of airbreathing propulsion at very high Mach numbers.

In broad terms, plasma-based control techniques include 1) injection of high-temperature air or plasma, for example, Ref. 1; 2) deposition of energy[2]; and 3) the imposition of external electromagnetic forces.[3] These flow control proposals have been brought into sharp focus as various components of the AJAX hypersonic concept vehicle.[4] Recent studies on the first two approaches have primarily addressed control of external flows, a blunt body is typically employed for analysis, and a vigorous debate has been established with

regard to the mechanisms underlying the apparent striking reduction in surface loads.[5]

The present effort is centered on the last of the preceding approaches in which the dominant control agents are the Lorentz forces and Joule heating phenomena. Although the use of magnetic fields to control external flows is not new, recent research has highlighted the considerable advantage that may be gained in scramjet operation. These ideas are incorporated into the so-called magnetohydrodynamic (MHD) energy bypass concept,[4,6] which essentially involves MGD-based extraction of energy from the inlet to provide a more benign and homogeneously mixed fuel–air mixture to the combuster, than if equivalent flow deceleration were accomplished with shock waves. The extracted energy can then be utilized for other onboard functions or to obtain additional thrust through MHD acceleration in the nozzle. Several thermodynamic analyses, some including energy budgets to maintain required conductivity levels, have explored the feasibility of the MHD energy-bypass concept and have established broad parameters under which benefits may be realized.[7,8]

The overall objective of the current effort is to develop simulation tools of increasing physical fidelity to aid in the process of understanding the mechanisms involved and to complement experimental programs to further explore the parameter space. The difficulty in numerical simulation stems from the highly multidisciplinary nature of the phenomena, which require coupling of the Maxwell and compressible Navier–Stokes equations and include nonideal considerations.

Realistic modeling of practical configurations demands the utilization of a fully three-dimensional technique, to satisfy not only geometrical constraints but also those dictated by the physics of the flow. Concerning fluid dynamics, relatively long scramjet designs mandated by fuel–air mixing requirements guarantee the existence of swept shock–boundary-layer interactions, complex vortical structures, and three-dimensional flow separation in the general case. These phenomena are fundamentally different in three-dimensions than in two-dimensions and determining their significant influence on the important performance and operational criteria demand fully three-dimensional simulations. Similarly, plasmadynamic mechanisms also require three-dimensional resolution: Lower-dimensional analyses may yield spurious solutions[9] and may neglect effects associated with Hall currents and variable transport properties (see Ref. 10).

Several recent publications[11–13] have addressed algorithm and tool development for MGD. In our own previous effort,[14] a spectrum of high-order Pade-type schemes was employed to solve the general three-dimensional nonideal MGD equations, with no constraints on the magnetic Reynolds number $Re_\sigma = \mu_m \sigma_{\text{ref}} U_{\text{ref}} L_{\text{ref}}$, where μ_m is the magnetic permeability of free space, U is the freestream velocity, L is a length scale, and subscript ref denotes a reference value. To establish the starting point for the present paper, this baseline formulation and scheme are summarized in Sec. II. The current effort advances the physical fidelity and numerical efficiency of that solution procedure.

Practical aerospace application of MHD control necessarily involve wall-bounded flows, which require fine, highly stretched near-wall meshes to resolve high local gradients. In these situations, explicit methods such as the Runge–Kutta methods, employed in Ref. 14, exhibit severe time-step-size limitations and are not efficient. To address this, a loosely coupled, approximately factored implicit method is developed in Sec. III, based on the classical approach of Ref. 15. Both first- and second-order time accuracy are obtained by encapsulating the method into a subiteration strategy, which minimizes errors associated with linearization, approximate factorization, and lagged boundary condition implementation. The accuracy and efficiency of the method is established by considering wave propagation and diffusion phenomena on curvilinear meshes.

The environment for aerospace flow control of the type listed earlier is characterized by low electrical conductivities and high magnetic fields.[8] These constraints may be specified in terms of nondimensional parameters, magnetic Reynolds number Re_σ and the magnetic pressure number $R_b = B_{\text{ref}}^2/(\mu_m \rho_{\text{ref}} U_{\text{ref}}^2)$, where B is the magnetic field strength, as $Re_\sigma \ll 1$ and $R_b \gg 1$. Although the governing equations employed in Ref. 14 are analytically well behaved in this regime, numerical problems are encountered both in terms of stability and accuracy. To alleviate these problems, a compressible low-magnetic-Reynolds-number Re_σ approximation, suitable for aerospace application, is described in Sec. III together with an associated numerical procedure. The formulation is verified by comparing with similarity solutions derived for high-speed flat-plate boundary-layer flows subjected to a specific applied magnetic field.[16]

Turbulence is an important feature of most flows of practical interest and is likely to be an important consideration in many regions of the hypersonic flight envelope, particularly in internal situations. Although the impact of the magnetic field on turbulence is extremely complex,[17] recent efforts have attempted to mimic fine-scale effects within the context of engineering approaches[18,19] by adapting developments from the field of metallurgy, where control with magnetic fields is more mature. A particularly attractive two-equation $k-\epsilon$ model has been developed in Ref. 20 to treat the effect of the magnetic field with only one additional closure coefficient. The method is based on Reynolds-stress analyses and provides a firm footing to some of the considerations employed earlier in Ref. 21. The extension to compressible flows, and implementation within the loosely coupled strategy outlined in Sec. II is described in Sec. V. Validation is accomplished for the no-MGD case, and calculations are presented to explore the effect of a magnetic dipole placed beneath a turbulent supersonic boundary layer.

The formulation and method is described and implemented for the fully three-dimensional situation. To demonstrate application to a complex flowfield, the paper concludes after describing an exploratory simulation of flow past a complete reentry configuration (Sec. VI), in which magnetic dipoles are placed at locations where load mitigation may be beneficial.

II. Baseline Model

The model employed in Ref. 14 is summarized to provide the baseline for subsequent enhancement. Combining the Navier–Stokes and pre-Maxwell equations together with Ohm's law, the governing equations are as follows.

Continuity equation:

$$\frac{\partial \rho^*}{\partial t^*} + \nabla \cdot (\rho^* \boldsymbol{U}^*) = 0 \tag{1}$$

Momentum equation:

$$\frac{\partial \rho^* \boldsymbol{U}^*}{\partial t^*} + \nabla \cdot \left[\rho^* \bar{\bar{U}}^* \boldsymbol{U}^* - R_b \frac{\bar{\bar{B}}^* \boldsymbol{B}^*}{\mu_m} + P^* \bar{\bar{I}} \right] - \frac{1}{Re} \nabla \cdot \bar{\bar{\tau}}^* = 0 \tag{2}$$

Energy equation:

$$\frac{\partial \rho^* Z^*}{\partial t^*} + \nabla \cdot \left[(\rho^* Z^* + P^*) \boldsymbol{U} - R_b \boldsymbol{B}^* \left(\boldsymbol{U}^* \cdot \frac{\boldsymbol{B}^*}{\mu_m^*} \right) \right.$$
$$- \frac{1}{Re} (\boldsymbol{U}^* \cdot \bar{\bar{\tau}}^*) - \frac{1}{(\gamma - 1) Pr M^2 Re} Q_{ht}^*$$
$$\left. + \frac{R_b}{R_\sigma} \left(\frac{\boldsymbol{B}^*}{\mu_m^* \sigma^*} \cdot \nabla \frac{\bar{\bar{B}}^*}{\mu_m^*} - \nabla \frac{\bar{\bar{B}}^*}{\mu_m^*} \cdot \frac{\boldsymbol{B}^*}{\mu_m^* \sigma^*} \right) \right] = 0 \tag{3}$$

Induction equation:

$$\frac{\partial \boldsymbol{B}^*}{\partial t^*} + \nabla \cdot (\bar{\bar{U}}^* \boldsymbol{B}^* - \bar{\bar{B}}^* \boldsymbol{U}^*) + \frac{1}{Re_\sigma} \nabla \times \left[\frac{1}{\sigma^*} \left(\nabla \times \frac{\boldsymbol{B}^*}{\mu_m^*} \right) \right] = 0 \tag{4}$$

where the superscript $*$ denotes a nondimensional quantity. $\boldsymbol{U}^* = \{u^*, v^*, w^*\}$ is the velocity vector, $\boldsymbol{B}^* = \{B_x^*, B_y^*, B_z^*\}$ is the magnetic induction vector, μ_m is the magnetic permeability of free space, and the following definitions hold:

$$P^* = p^* + R_b \left(\boldsymbol{B}^{*^2} / 2\mu_m^* \right) \tag{5}$$

$$Z^* = [p^*/(\gamma-1)\rho^*] + \left(\boldsymbol{U}^{*^2}/2\right) + R_b\left(\boldsymbol{B}^{*^2}/2\mu_m^*\rho^*\right) \quad (6)$$

where $\boldsymbol{B}^{*^2} = \boldsymbol{B}^* \cdot \boldsymbol{B}^*$, $\boldsymbol{U}^{*^2} = \boldsymbol{U}^* \cdot \boldsymbol{U}^*$, p is the static pressure, $\bar{\bar{\tau}}$ is the stress tensor,[22] and, in terms of temperature T, $Q_{\text{ht}}^* = k^* \bigtriangledown T^*$.

The nondimensional variables are

$$t^* = tU_{\text{ref}}/L, \qquad \rho^* = \rho/\rho_{\text{ref}}, \qquad U^* = U/U_{\text{ref}}$$

$$B^* = B/B_{\text{ref}}, \qquad p^* = p\Big/\rho_{\text{ref}}U_{\text{ref}}^2, \qquad \mu_m^* = \mu_m/\mu_{m_{\text{ref}}}$$

$$\mu^* = \mu/\mu_{\text{ref}}, \qquad \sigma^* = \sigma/\sigma_{\text{ref}}, \qquad T^* = T/T_{\text{ref}} \quad (7)$$

In addition to magnetic Reynolds number Re_σ and R_b introduced earlier, other nondimensional parameters include the Reynolds number $Re = \rho_{\text{ref}}U_{\text{ref}}L_{\text{ref}}/\mu_{\text{ref}}$, the Prandtl number $Pr = \mu_{\text{ref}}C_p/k_{\text{ref}} = 0.72$, and the Mach number $M = U_{\text{ref}}/\sqrt{(\gamma p_{\text{ref}}/\rho_{\text{ref}})}$. The current $\boldsymbol{j}$ implicit in the preceding equations is normalized with $B_{\text{ref}}/(\mu_m L_{\text{ref}})$. Thus,

$$\boldsymbol{j}^* = \bigtriangledown \times \left(\boldsymbol{B}^*/\mu_m^*\right) = Re_\sigma \sigma^*(\boldsymbol{E}^* + \boldsymbol{U}^* \times \boldsymbol{B}^*) \quad (8)$$

where $\boldsymbol{E}^* = \boldsymbol{E}/(U_{\text{ref}}B_{\text{ref}})$. Note that Hall effect, ion-slip, and electron pressure terms have been suppressed in the preceding version of Ohm's law. The first two effects are likely to be important in applications of aerospace interest, and their contributions to the formulation, the conductivity is a tensor in this case, have been presented in Ref. 18 but are suppressed here because they have no direct implication on the developments described in the present work.

In the subsequent discussion, the superscript $*$ will be dropped, and all quantities will be assumed to be nondimensional unless explicitly otherwise stated.

The governing equations may be written in flux vector form as

$$\frac{\partial \boldsymbol{X}}{\partial t} + \frac{\partial \boldsymbol{F}_I}{\partial x} + \frac{\partial \boldsymbol{G}_I}{\partial y} + \frac{\partial \boldsymbol{H}_I}{\partial z} = \frac{\partial \boldsymbol{F}_V}{\partial x} + \frac{\partial \boldsymbol{G}_V}{\partial y} + \frac{\partial \boldsymbol{H}_V}{\partial z} + \boldsymbol{S} \quad (9)$$

where $\boldsymbol{X}$ is the solution vector, $\boldsymbol{X} = \{\rho, \rho u, \rho v, \rho w, \rho Z, B_x, B_y, B_z\}$, $\boldsymbol{F}_I$, $\boldsymbol{G}_I$, and $\boldsymbol{H}_I$ contain terms relevant to inviscid, perfectly conducting media, whereas $\boldsymbol{F}_V$, $\boldsymbol{G}_V$, and $\boldsymbol{H}_V$ include effects due to viscosity and finite electrical conductivity. The various vectors of Eq. (9), where the source term S is identically zero in this formulation, have been detailed in Ref. 14 and are not repeated here. To treat physically complex domains, the preceding governing equations are extended to curvilinear coordinates in the standard manner[22] by introducing the transformation $x = x(\xi, \eta, \zeta)$, $y = y(\xi, \eta, \zeta)$, and $z = z(\xi, \eta, \zeta)$. The strong conservation form is employed to obtain

$$\frac{\partial \hat{\boldsymbol{X}}}{\partial t} + \frac{\partial \hat{\boldsymbol{F}}_I}{\partial \xi} + \frac{\partial \hat{\boldsymbol{G}}_I}{\partial \eta} + \frac{\partial \hat{\boldsymbol{H}}_I}{\partial \zeta} = \frac{\partial \hat{\boldsymbol{F}}_V}{\partial \xi} + \frac{\partial \hat{\boldsymbol{G}}_V}{\partial \eta} + \frac{\partial \hat{\boldsymbol{H}}_V}{\partial \zeta} + \hat{\boldsymbol{S}} \quad (10)$$

where, with J representing the Jacobian of the transformation, $\hat{\boldsymbol{X}} = \boldsymbol{X}/J$, $\hat{\boldsymbol{S}} = \boldsymbol{S}/J$, and

$$\hat{\boldsymbol{F}}_I = (1/J)(\xi_x \boldsymbol{F}_I + \xi_y \boldsymbol{G}_I + \xi_z \boldsymbol{H}_I)$$

$$\hat{\boldsymbol{F}}_V = (1/J)(\xi_x \boldsymbol{F}_V + \xi_y \boldsymbol{G}_V + \xi_z \boldsymbol{H}_V)$$

with similar expressions for $\hat{\boldsymbol{G}}_I$, $\hat{\boldsymbol{G}}_V$, etc.

A spectrum of high-order centered schemes is employed to solve the earlier governing equations.[14] In these, the derivative of each required quantity, for example, ϕ, is obtained in the uniformly discretized transformed plane (ξ, η, ζ) with the formula

$$\Gamma\phi'_{i-1} + \phi'_i + \Gamma\phi'_{i+1} = b[(\phi_{i+2} - \phi_{i-2})/4] + a[(\phi_{i+1} - \phi_{i-1})/2] \quad (11)$$

where Γ, a, and b determine the spatial properties of the algorithm. Popular schemes include the fourth-order three-point scheme, C4, for which $\Gamma = \frac{1}{4}$, $a = \frac{3}{2}$, $b = 0$, and the standard explicit second-order scheme, E2, for which $\Gamma = 0$, $a = 1$, and $b = 0$. Details of the spectral characteristics of these schemes, and others obtainable from Eq. (11), may be found in Refs. 23 and 24.

The derivatives of the inviscid fluxes are obtained by first forming these fluxes at the nodes and subsequently differentiating each component with the described technique. To form terms containing the molecular viscosity μ and electrical conductivity σ, the primitive variables u, v, w, T, B_x, B_y, and B_z, are first differentiated and properly combined with the transport coefficients to form the requisite combinations of first derivative terms. These gradients are then differentiated again. To reduce the error on stretched meshes, the required metrics are computed in the same manner as the fluxes.[24] An extensive discussion of the metric evaluation procedures for higher-order techniques may be found in Ref. 25.

Additional components are required in the method to enforce numerical stability, which can be compromised by mesh stretching, boundary condition implementation, and nonlinear phenomena. Two methods are employed to stabilize the calculations. In the first, spurious frequencies in the solution are systematically removed with a filter designed using spectral analysis. Details of this component may be found in Ref. 24. In cases where relatively strong steady shock fronts are present, the filtering procedure is unacceptably diffusive. In such cases, a blend of second- and fourth-order spectral dissipation is employed as described in Ref. 26 for the non-MGD case. For MGD, the solution vector is extended to include rows corresponding to the $\boldsymbol{B}$ field. The same acoustic spectral radius as applied in non-MHD applications is retained because numerical experiments with the fast magnetoacoustic wave speed do not indicate any significant advantage for the problems under study.

Physical boundary conditions are applied after each update of the interior solution vector. These include Dirichlet (no-slip) and Neumann, for example, $\partial p/\partial n = 0$, extrapolation, and symmetry, conditions and, because they are problem dependent, are discussed in later sections.

For initial conditions, uniform flow is assumed, and the $\boldsymbol{B}$ field is chosen to satisfy $\bigtriangledown \cdot \boldsymbol{B} = 0$. The constrained transport method is employed, and solutions are marched in time-accurate fashion to minimize the development of spurious magnetic field divergence. In previous efforts,[27,28] the fourth-order classical Runge–Kutta (RK4) method (see Ref. 29) has been utilized. The implementation of an approximately factored implicit Beam–Warming method[30] is described subsequently.

III. Implicit Time Integration

Explicit time-integration schemes, such as the Runge–Kutta method utilized in Ref. 28, typically suffer severe time-step-size limitations, especially in wall-bounded flows, where boundary mesh spacing is tight and large stretch factors are typically necessary. To overcome this limitation, an implicit method has been incorporated with a subiteration technique, similar to that described in Ref. 31 for the Navier–Stokes equations. The basic formula to compute the change in the solution vector $\Delta\boldsymbol{X}$ is

$$\left[J^{-1} + \frac{1}{1+\phi}\Delta t \quad \delta_\xi \hat{A}^p\right] J \times \left[J^{-1} + \frac{1}{1+\phi}\Delta t \quad \delta_\eta \hat{B}^p\right] \times J$$

$$\times \left[J^{-1} + \frac{1}{1+\phi}\Delta t \quad \delta_\zeta \hat{C}^p\right] \Delta\boldsymbol{X} = -\frac{1}{1+\phi}\Delta t$$

$$\times \left[J^{-1}\frac{(1+\phi)\boldsymbol{X}^p - (1+2\phi)\boldsymbol{X}^n + \phi\boldsymbol{X}^{n-1}}{\Delta t} + \hat{R}^p\right] \quad (12)$$

where Δt is the time-step size, δ_ξ, δ_η, and δ_ζ denote central second-order derivative operators, and ϕ controls the order of accuracy of the scheme: In this effort, we consider first- and second-order approaches with $\phi = 0$ and $\frac{1}{2}$, respectively. $\hat{A}$, $\hat{B}$, and $\hat{C}$ are transformed flux Jacobians, for example, $\hat{A} = \partial(\hat{\boldsymbol{F}}_I + \hat{\boldsymbol{F}}_V)/\partial\boldsymbol{X}$, and $\hat{R}$ is the residual evaluated with the high-order compact-difference method. The superscript p represents the subiteration counter starting at $p = 0$ for the first subiteration at which stage $\boldsymbol{X}^p = \boldsymbol{X}^n$ and as $p \to \infty$, $\boldsymbol{X}^p \to \boldsymbol{X}^{n+1}$. Subiterations reduce linearization, factorization, and explicit boundary condition implementation errors and also permit the use of second-order spatial operators on the left-hand side of the equation. Typically, at most two or three subiterations

suffice to achieve inner-iteration convergence. Equation (12) also includes nonlinear artificial dissipation terms,[26] which are added to the implicit operator to enhance stability. Spectrally scaled second- and fourth-order solution vector difference operators, extended to include rows corresponding to the B field, are added with pressure-based switches. The same acoustic spectral radius as applied in non-MHD applications is retained because numerical experiments with the fast magnetoacoustic wave speed do not indicate any significant advantage for the problems under study.

In evaluating the flux Jacobians, several simplifications have been invoked to improve the efficiency of the numerical algorithm. Without these, the factorization of Eq. (12) requires inversion of tridiagonal matrices comprised of 8×8 blocks. Because this effort scales as the third power of the dimension, here we split the solution procedure into two parts, one to obtain new values of the vector comprising of the first five components of $\boldsymbol{X}$, $\boldsymbol{X}_f = \{\rho, \rho u, \rho v, \rho w, \rho Z\}$ and the other for the last three, $\boldsymbol{X}_m = \{B_x, B_y, B_z\}$. Thus, the two systems solved are

$$\left[J^{-1} + \frac{1}{1+\phi}\Delta t \quad \delta_\xi \hat{A}_f^p\right] J \cdot \left[J^{-1} + \frac{1}{1+\phi}\Delta t \quad \delta_\eta \hat{B}_f^p\right] \times J \times \left[J^{-1} + \frac{1}{1+\phi}\Delta t \quad \delta_\zeta \hat{C}_f^p\right] \Delta \boldsymbol{X}_f = -\frac{1}{1+\phi}\Delta t \times \left[J^{-1}\frac{(1+\phi)\boldsymbol{X}_f^p - (1+2\phi)\boldsymbol{X}_f^n + \phi \boldsymbol{X}_f^{n-1}}{\Delta t} + \hat{\boldsymbol{R}}_f^p\right]$$

$$\left[J^{-1} + \frac{1}{1+\phi}\Delta t \quad \delta_\xi \hat{A}_m^p\right] J \cdot \left[J^{-1} + \frac{1}{1+\phi}\Delta t \quad \delta_\eta \hat{B}_m^p\right] \times J \times \left[J^{-1} + \frac{1}{1+\phi}\Delta t \quad \delta_\zeta \hat{C}_m^p\right] \Delta \boldsymbol{X}_m = -\frac{1}{1+\phi}\Delta t \times \left[J^{-1}\frac{(1+\phi)\boldsymbol{X}_m^p - (1+2\phi)\boldsymbol{X}_m^n + \phi \boldsymbol{X}_m^{n-1}}{\Delta t} + \hat{\boldsymbol{R}}_m^p\right] \tag{13}$$

where $\hat{\boldsymbol{R}}_f$ and $\hat{\boldsymbol{R}}_m$ are column vectors of the first five and remaining three components, respectively, of the residual, and $\hat{A}_f$, $\hat{A}_m$, $\hat{B}_f$, etc., are submatrices of $\hat{A}$, $\hat{B}$, and $\hat{C}$, respectively, as will be detailed. This approach is shown schematically in Fig. 1; note that the two subvectors, $\boldsymbol{X}_f$ and $\boldsymbol{X}_m$ are updated simultaneously. The alternative procedure of updating one first and utilizing the updated values in computing the other was not explored; however, see Sec. V.

The flux Jacobians $\hat{A}_f$, $\hat{A}_m$, etc., contain terms due to both the inviscid (subscript I) and viscous fluxes (subscript V) and may be derived analytically. For brevity, details are given only for $\hat{A}_f$ and $\hat{A}_m$, with the understanding that a parallel development may be employed to obtain the other blocks:

$$\hat{A}_f \Delta \boldsymbol{X}_f = \hat{A}_{f,I} \Delta \boldsymbol{X}_f + \hat{A}_{f,V} \Delta \boldsymbol{X}_f = \Delta \hat{\boldsymbol{F}}_{f,I} + \Delta \hat{\boldsymbol{F}}_{f,V} \tag{14}$$

where $\hat{\boldsymbol{F}}_{f,I}$ and $\hat{\boldsymbol{F}}_{f,V}$ are the first five components of $\hat{\boldsymbol{F}}_I$ and $\hat{\boldsymbol{F}}_V$ [Eqs. (25) and (26)], respectively. $J\hat{A}_{f,I}$ may be written as

$$\begin{bmatrix} 0 & \xi_x & \xi_y & \xi_z & 0 \\ \xi_x(\gamma-1)\alpha - uU & U - \xi_x(\gamma-2)u & \xi_y u - \xi_x(\gamma-1)v & \xi_z u - \xi_x(\gamma-1)w & \xi_x(\gamma-1) \\ \xi_y(\gamma-1)\alpha - vU & \xi_x v - \xi_y(\gamma-1)u & V - \xi_y(\gamma-2)v & \xi_z v - \xi_y(\gamma-1)w & \xi_y(\gamma-1) \\ \xi_z(\gamma-1)\alpha - wU & \xi_x w - \xi_z(\gamma-1)u & \xi_y w - \xi_z(\gamma-1)v & W - \xi_z(\gamma-2)w & \xi_z(\gamma-1) \\ \hat{a}_{51_{f,I}} & \hat{a}_{52_{f,I}} & \hat{a}_{53_{f,I}} & \hat{a}_{54_{f,I}} & \gamma U \end{bmatrix} \tag{15}$$

where

$$\hat{a}_{51_{f,I}} = -\gamma p/(\gamma-1)\rho + (\gamma-2)\alpha U - (R_b/\rho\mu_m)[U(\boldsymbol{B}\cdot\boldsymbol{B}) - B(\boldsymbol{U}\cdot\boldsymbol{B})]$$

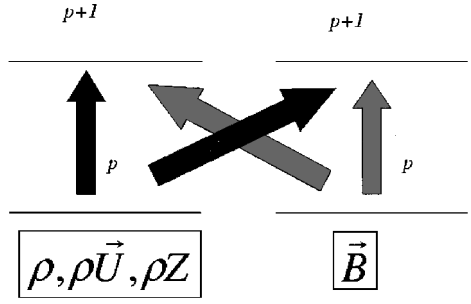

Fig. 1 Schematic of decoupled implicit time integration: p = subiteration level.

$$\hat{a}_{52_{f,I}} = \xi_x[1/(\gamma-1)](\gamma p/\rho + \gamma\alpha) - (\gamma-1)uU + (R_b/\rho\mu_m)(\xi_x \boldsymbol{B}\cdot\boldsymbol{B} - B_x B)$$

$$\hat{a}_{53_{f,I}} = \xi_y[1/(\gamma-1)](\gamma p/\rho + \gamma\alpha) - (\gamma-1)vU + (R_b/\rho\mu_m)(\xi_y \boldsymbol{B}\cdot\boldsymbol{B} - B_y B)$$

$$\hat{a}_{54_{f,I}} = \xi_z[1/(\gamma-1)](\gamma p/\rho + \gamma\alpha) - (\gamma-1)wU + (R_b/\rho\mu_m)(\xi_z \boldsymbol{B}\cdot\boldsymbol{B} - B_z B)$$

$$\alpha = \tfrac{1}{2}(u^2+v^2+w^2), \qquad B = \xi_x B_x + \xi_y B_y + \xi_z B_z$$

$$U = \xi_x u + \xi_y v + \xi_z w$$

Note that these blocks are the three-dimensional curvilinear coordinate equivalents of those in Ref. 32, and if the magnetic field is set to zero, these expressions revert to those encountered in traditional fluid dynamics.[33]

For the viscous components, the simplifications described in Ref. 15 for the Navier–Stokes equations have been invoked. First, to compute the flux Jacobians, the thin-layer approximation is utilized. Thus, all cross-derivative terms are suppressed. Functionally,

$$\hat{\boldsymbol{F}}_{f,V} = \hat{\boldsymbol{F}}_{f,V}(\boldsymbol{X}_f, \boldsymbol{X}_{f,\xi}) \tag{16}$$

$$\Delta\hat{\boldsymbol{F}}_{f,V} = \frac{\partial \hat{\boldsymbol{F}}_{f,V}}{\partial \boldsymbol{X}_f}\Delta\boldsymbol{X}_f + \frac{\partial \hat{\boldsymbol{F}}_{f,V}}{\partial \boldsymbol{X}_{f,\xi}}\Delta\boldsymbol{X}_{f,\xi} = \hat{P}_{f,V}\Delta\boldsymbol{X}_f + \hat{Q}_{f,V}\Delta\boldsymbol{X}_{f,\xi} = (\hat{P}_{f,V} - \hat{Q}_{f,V,\xi})\Delta\boldsymbol{X}_f + \frac{\partial}{\partial\xi}(\hat{Q}_{f,V}\Delta\boldsymbol{X}_f) \tag{17}$$

where the subscript ξ denotes differentiation with respect to ξ. It is further assumed that the term $\hat{P}_{f,V} - \hat{Q}_{f,V_\xi}$ is negligible: The primary requirements for this are that the transport properties do not exhibit significant local spatial variation and are not dependent on the solution vector. Note again that none of these assumptions affects the modeling detail of the final result because, within the subiteration approach, the accuracy is determined by the residual, which utilizes all terms in the governing equations. The only block required then is $\hat{Q}_{f,V}$, which may be written as

$$\hat{Q}_{f,V} = \frac{1}{Re}\begin{bmatrix} 0 & 0 & 0 & 0 & 0 \\ -\frac{\mu}{\rho}\left[\frac{4}{3}\xi_x u - \frac{2}{3}(\xi_y v + \xi_z w)\right] & \frac{4\mu}{3\rho}\xi_x & -\frac{2}{3\rho}\xi_y & -\frac{2}{3\rho}\xi_z & 0 \\ -\frac{\mu}{\rho}(\xi_y u + \xi_x v) & \frac{\mu}{\rho}\xi_y & \frac{\mu}{\rho}\xi_x & 0 & 0 \\ -\frac{\mu}{\rho}(\xi_z u + \xi_x w) & \frac{\mu}{\rho}\xi_z & 0 & \frac{\mu}{\rho}\xi_x & 0 \\ r_{51} & r_{52} & r_{53} & r_{54} & \frac{\mu\xi_x}{Pr}\gamma\left(\frac{1}{\rho}\right) \end{bmatrix} \tag{18}$$

$$r_{51} = u \times [2,1] + v \times [3,1] + w \times [4,1] + \frac{\mu\xi_x}{Pr(\gamma-1)}\left(\frac{\gamma}{\rho}\right)\left(-\frac{p}{\rho} + \phi\right), \qquad r_{52} = u \times [2,2] + v \times [3,2] + w \times [4,2] + \frac{\mu\xi_x}{Pr}(-\gamma)\left(\frac{u}{\rho}\right)$$

$$r_{53} = u \times [2,3] + v \times [3,3] + w \times [4,3] + \frac{\mu\xi_x}{Pr}(-\gamma)\left(\frac{v}{\rho}\right), \qquad r_{54} = u \times [2,4] + v \times [3,4] + w \times [4,4] + \frac{\mu\xi_x}{Pr}(-\gamma)\left(\frac{w}{\rho}\right)$$

where terms in brackets are the corresponding elements of the array $\hat{Q}_{f,V}$ and $\phi = (\gamma - 1)\alpha$.

The matrices $\hat{A}_{m,I}$, $\hat{Q}_{m,V}$, etc., may be obtained in similar fashion:

$$\hat{A}_{m,I} = \begin{bmatrix} v\xi_y + w\xi_z & -u\xi_y & -u\xi_z \\ -v\xi_x & u\xi_x + w\xi_z & -v\xi_z \\ -w\xi_x & -w\xi_y & u\xi_x + v\xi_y \end{bmatrix} \tag{19}$$

and the matrix $\boldsymbol{R}_{m,V}$ is

$$\boldsymbol{R}_{m,V} = \frac{1}{\sigma Re_\sigma}\begin{bmatrix} \xi_y^2 + \xi_z^2 & -\xi_x\xi_y & -\xi_x\xi_z \\ -\xi_x\xi_y & \xi_x^2 + \xi_z^2 & -\xi_x\xi_z \\ \xi_x\xi_z & \xi_y\xi_z & \xi_x^2 + \xi_y^2 \end{bmatrix} \tag{20}$$

One consequence of solving for the magnetic field separately is that the Joule heating term is effectively treated explicitly. Although this likely impacts the overall stability of the scheme, several computations (some presented subsequently) demonstrate the significant stability gain of the new approach.

The accuracy and efficiency of the implicit time-accurate scheme are demonstrated with two sample calculations, the first addressing a diffusion process and the second a wave propagation phenomenon in the presence of Ohmic damping. The schematic of the MHD equivalent of the Rayleigh problem in fluid dynamics is shown in Fig. 2a. It consists of a finitely conducting semi-infinite region (constant σ) bounded on one side by an infinite surface on which a current sheet is suddenly imposed in the z direction. With neither macroscopic fluid movement nor a B_y component, that is, no Alfven waves are generated, the induced magnetic field B_x and current j_z diffuse in the direction of nonuniformity, y. The problem is amenable to analytic solution in terms of the complimentary error function as described in Ref. 27. The second-order time-integration scheme is employed with the C4 spatial scheme. Figure 2b shows the adequacy of the mesh and time-step size employed and also a comparison of the efficiency of the implicit method with the explicit RK4 scheme. To highlight the advantages of the implicit scheme, these computations were performed on two highly stretched meshes with minimum plate-normal spacings of 0.005 and 0.0025 and mesh points $11 \times 51 \times 11$ and $11 \times 101 \times 11$, respectively. Although all computations, plotted at time $T = 0.5$, are in excellent agreement with theory, the time-step size employed with the implicit scheme is three orders of magnitude higher than with the explicit scheme (which is operated at its highest stable time-step-size value). In terms of computational expense, one iteration of the implicit scheme requires only 5% more computation time than the RK4 method. This relative similarity is a consequence of the fact that, despite the requirement in the former to invert block tridiagonal matrices, the

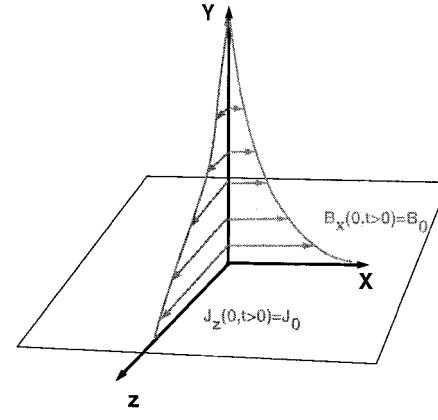

a) Schematic

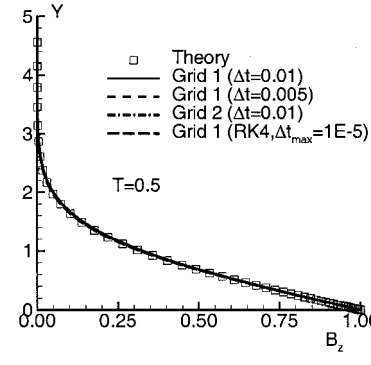

b) Grid and time-step-size study

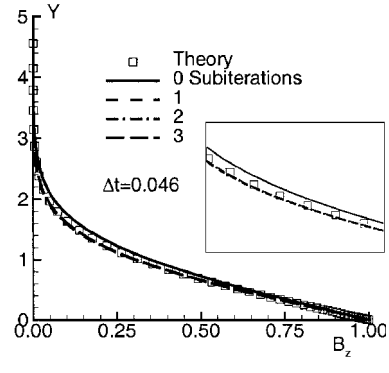

c) Effect of subiteration

Fig. 2 Accuracy and efficiency of implicit technique on diffusion problem.

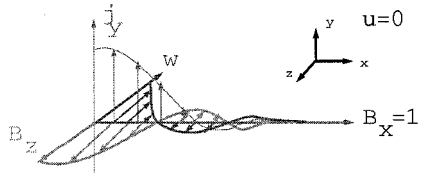

a) Schematic

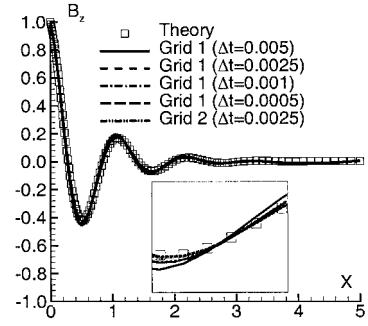

c) Effect of time-step and grid size

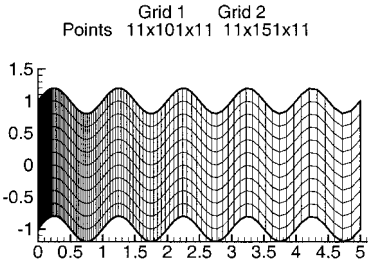

b) Grid

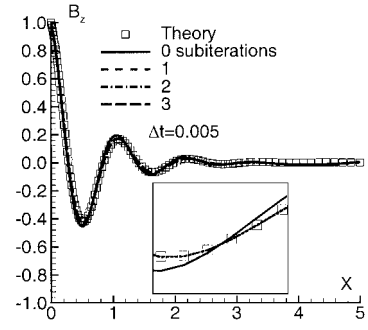

d) Effect of subiterations

Fig. 3 Performance of implicit technique on Alfvén wave propagation with Ohmic damping.

latter needs four evaluations of the residual with the high-order Pade scheme. Although the residual computation can be simplified with explicit instead of Pade spatial schemes, previous efforts have shown that because of their spectral-like resolution, the latter are far more efficient in terms of the total number of grid points required.

Figure 2c explores the use of subiterations in recovering accuracy at a time-step size ($\Delta t = 0.046$) near the limit of numerical stability of the implicit scheme. At this high step size, the solution displays significant error with no subiterations. This deficiency is considerably diminished when one subiteration is employed (effectively doubling the required computation time). The small residual error is attributed to the basic second-order accuracy of the scheme, which, at a given step size and increasing subiterations, becomes the limiting factor determining overall accuracy. Because the computational effort is directly proportional to the number of subiterations employed, a tradeoff exists between more subiterations at high step sizes and fewer subiterations at lower step sizes. This aspect was not explored in the present effort.

A similar analysis is performed for a wave propagation problem shown schematically in Fig. 3, in which vorticity is generated, propagated with transverse Alfvén waves, and dissipated by the finitely conducting medium. In this case, a sinusoidally oscillating current sheet, at a frequency $\omega = 1$, is applied in the y direction on the $y - z$ plane at $x = 0$, yielding an induced $\boldsymbol{B}$ field in the z direction consistent with Ampere's law. The coordinate frame is oriented such that the streamwise velocity $u = 0$. However, unlike in the preceding problem, a unit magnetic field B_x is imposed. The transverse disturbance then travels and ultimately decays along the x direction. The analytic solution of the problem has been discussed in Ref. 17, and issues of numerical problem setup have been explored in Ref. 27.

Although a simple Cartesian grid is suitable, to examine the performance of the scheme on general meshes, a curvilinear, stretched grid is employed as shown in Fig. 3b. The minimum x spacing is 0.01 and 0.0075 on two meshes consisting of $101 \times 11 \times 11$ and $151 \times 11 \times 11$ points, respectively. The y-coordinate lines are varied in a smooth fashion with a sinusoidal wave as shown. Figure 3c shows results with various time-step sizes on the two meshes. The negligible difference in predictions with the two grids at the same time-step size, $\Delta t = 0.0025$, demonstrate the adequacy of the spatial resolution. Results on grid 1 at various step sizes illustrate the effect of time-step size on accuracy. At the highest Δt, significant error is evident. However, this error diminishes with reduced step size, and the distinction between $\Delta t = 0.001$ and 0.0005 is negligible (see inset, Fig. 3c). Figure 3d explores the use of subiterations to improve the solution accuracy at the relatively high step size of $\Delta t = 0.005$. The use of one subiteration yields significant improvement, and because the error is negligible, additional subiterations do not yield any perceptible change in solution. Computations have also been performed on the MGD shock tube case[34] with the new loosely coupled approach. Results with both first- and second-order implicit methods yield very good agreement with those obtained with the explicit RK4 method (see Ref. 14) but are not shown here for brevity.

IV. Source-Term Formulation

As noted earlier, the aerospace environment of interest is likely to be characterized by relatively low levels of conductivity.[8] This is particularly the case in external situations where artificial ionization techniques are difficult to implement. The pertinent nondimensional parameter determining the relative magnitude of σ is the magnetic Reynolds number introduced earlier. In the limit $Re_\sigma \to 0$, Eqs. (3) and (4) are well behaved analytically even though magnetic Reynolds number Re_σ appears in the denominator of some terms because the numerator approaches zero more rapidly. For example, the derivation of Eq. (3) shows that the last term is actually proportional to $\boldsymbol{j}^2/\sigma$, which, from the nondimensional form of Ohm's law, is proportional to magnetic Reynolds number Re_σ. From a numerical standpoint, however, terms involving magnetic Reynolds number Re_σ are problematic because their proper evaluation requires ratios of relatively small quantities, some of which are obtained discretely. Terms involving R_b on the other hand are numerically well behaved in the limit $Re_\sigma \to 0$ and decouple the magnetic field from the fluid flow by virtue of the fact that the divergence of the Maxwell stress tensor vanishes. However, accuracy considerations continue to be important if R_b is large because small errors in the evaluation of the Maxwell stresses can translate into large body forces. To alleviate these problems, considerable simplification can be achieved by recognizing that the induced magnetic field is negligible when magnetic Reynolds number Re_σ is small.[17] In this case, Ampere's law is suppressed, and the current is obtained directly from Ohm's law. Under these conditions, it is more practical to express the electromagnetic

force as a source term to the Navier–Stokes equations. The nondimensional equations are then (with $*$ reintroduced)

$$\frac{\partial \rho^*}{\partial t^*} + \nabla^* \cdot (\rho^* \boldsymbol{U}^*) = 0 \tag{21}$$

$$\frac{\partial \rho^* \boldsymbol{U}^*}{\partial t^*} + \nabla^* \cdot [\rho^* \bar{\bar{U}}^* \boldsymbol{U}^* + p^* \bar{\bar{I}}] - \frac{1}{Re} \nabla^* \cdot \bar{\bar{\tau}}^* = R_b Re_\sigma \boldsymbol{j}^* \times \boldsymbol{B}^* \tag{22}$$

$$\frac{\partial \rho^* e^*}{\partial t^*} + \nabla^* \cdot \left[(\rho^* e + p^*) \boldsymbol{U}^* - \frac{1}{Re} (\boldsymbol{U}^* \cdot \bar{\bar{\tau}}^*) - \frac{1}{(\gamma - 1) PrM^2 Re} Q^*_{\text{ht}} \right] = R_b Re^*_\sigma \boldsymbol{E}^* \cdot \boldsymbol{j}^* \tag{23}$$

where $e^* = p^*/(\gamma - 1)\rho^* + \boldsymbol{U}^{*^2}/2$. In this form of the governing equations, the electromagnetic quantities, $\boldsymbol{B}^*$, $\boldsymbol{j}^*$, and $\boldsymbol{E}^*$ appear only in the source terms on the right side of the equation. Because the induced magnetic field is small, $\boldsymbol{B}^*$ is the imposed value that is specified, and the current vector $\boldsymbol{j}^*$ is obtained from Ohm's law.

The electric field is obtained by first introducing a scalar potential ϕ through the relation $\boldsymbol{E}^* = \nabla \cdot \phi^*$ and enforcing the current continuity constraint, $\nabla \cdot \boldsymbol{j}^* = 0$. Thus, although Ampere's law is suppressed in the source-term formulation, its consequence, that current flows in closed loops, is retained.[35] The governing equation for ϕ is then

$$\nabla \cdot [\sigma \cdot (-\nabla \phi + \boldsymbol{U} \times \boldsymbol{B})] = 0 \tag{24}$$

Details of the solution procedure, including tensor conductivity considerations, are described in Ref. 36. In all of the low-magnetic-Reynolds-number Re_σ cases considered here, no electric field is imposed, the induced electric field is either assumed negligible or is precisely zero, and the source term in the energy equation is zero. The quantity $R_b Re_\sigma = \sigma_{\text{ref}} B^2_{\text{ref}} L_{\text{ref}}/(\rho_{\text{ref}} U_{\text{ref}})$ is the magnetic interaction parameter and will be denoted as Q.

The low-magnetic-Reynolds-number Re_σ equations may also be written in the form of Eq. (9) and extended to curvilinear coordinates as in Eq. (10). However, the solution vector $\boldsymbol{X} = \{\rho, \rho u, \rho v, \rho w, \rho e\}$ (superscript $*$ suppressed) and the flux vectors $\boldsymbol{F}_I$, $\boldsymbol{G}_I$, ..., contain only five rows instead of the eight in the general formulation, yielding a considerable reduction in computational expense. For example, $\boldsymbol{F}_I$ and $\boldsymbol{F}_V$ are

$$\boldsymbol{F}_I = \begin{Bmatrix} \rho u \\ \rho u^2 + p \\ \rho uv \\ \rho uw \\ (\rho e + p)u \end{Bmatrix} \tag{25}$$

$$\boldsymbol{F}_V = \begin{Bmatrix} 0 \\ \frac{1}{Re}\tau_{xx} \\ \frac{1}{Re}\tau_{xy} \\ \frac{1}{Re}\tau_{xz} \\ \frac{1}{Re}(u\tau_{xx} + v\tau_{xy} + w\tau_{xz}) + \frac{1}{(\gamma - 1)PrM^2 Re}\frac{\partial T}{\partial x} \end{Bmatrix} \tag{26}$$

while the source term is no longer zero. When $\boldsymbol{j}$ is eliminated by using Ohm's law,

$$\boldsymbol{S} = \begin{Bmatrix} 0 \\ \{Q\sigma[B_z(E_y + wB_x - uB_z) - B_y(E_z + uB_y - vB_x)]\} \\ \{Q\sigma[B_x(E_z + uB_y - vB_x) - B_z(E_x + vB_z - wB_y)]\} \\ \{Q\sigma[B_y(E_x + vB_z - wB_y) - B_x(E_y + wB_x - uB_z)]\} \\ \{Q\sigma[E_x(E_x + vB_z - wB_y) + E_y(E_y + wB_x - uB_z) + E_z(E_z + uB_y - vB_x)]\} \end{Bmatrix} \tag{27}$$

The same method as employed for the general formulation can also address the low-magnetic-Reynolds-number Re_σ formulation. However, additional flexibility can be obtained by noting that the influence of the magnetic field is restricted exclusively to the source term and that the eigensystem of the corresponding homogeneous system is not afflicted by the degenerate eigenvalues found in MHD. (Magnetic field-specific wave phenomena are neglected.) Thus, it is straightforward and sometimes advantageous to employ more conventional computational fluid dynamics methods. Both the Roe[37] and van Leer schemes[38] have been incorporated together with the MUSCL scheme[38] to obtain up to nominal third-order accuracy. Solution monotonicity is assured with the harmonic limiter described in Ref. 39. For time integration, the implicit technique of Sec. III can be easily extended by including the Jacobian of the source term. When it is assumed that the electric field is frozen, the only variable is the velocity vector.

To verify implementation of the low-magnetic-Reynolds-number Re_σ formulation and to demonstrate the use of the implicit technique with a wall-bounded flow, consider a flat-plate boundary layer at the parameters summarized in Fig. 4a. The problem explores the

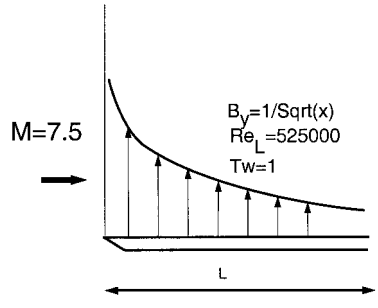

a) Schematic: T_w = wall temperature

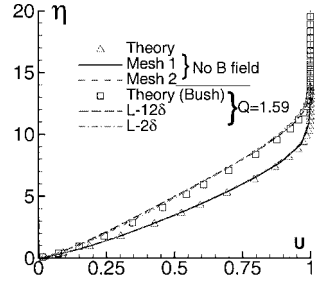

b) u-velocity profiles

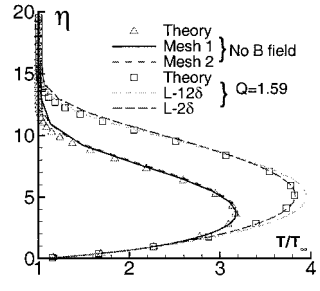

c) Temperature profiles

Fig. 4 MGD control of laminar supersonic flow past flat plate.

use of MGD control techniques to reduce skin-friction coefficient and heat transfer rates. The incoming flow is assumed to be at Mach 7.5, and the Reynolds number based on the length of the plate is fixed at 5.25×10^5. The primary aspects of the simulation are chosen to mimic the semi-analytic effort of Bush[16] to the best extent possible. The analysis assumes that the magnetic Reynolds number is small; thus, the low-magnetic-Reynolds-number formulation is appropriate. The Roe flux-difference split scheme is employed for the inviscid fluxes, whereas viscous terms are centered as in Ref. 14. The numerical simulation is compared with the analytic method of Ref. 16, which reduces the governing equations in the boundary layer to two ordinary differential equations of third order and are solved separately with a standard Runge–Kutta scheme and Newton–Raphson iteration. The value of the interaction parameter considered here is $Q = 1.59$. The electrical conductivity is represented by a power law:

$$\sigma = (T/T_\sigma)^n \tag{28}$$

where note that all quantities are nondimensionalized, including temperatures T and T_σ ($= 1.65$), which are both normalized by T_{ref}. The index n is fixed at 4.1. The effect of the imposed magnetic field is modeled exclusively through the vertical component B_y, which, again following Ref. 16, is chosen to vary along the surface as

$$B_y|_{\text{surface}} = 1/\sqrt{x} \tag{29}$$

Beyond this, in Ref. 16 it is assumed that $\partial B_y/\partial y = \mathcal{O}(1)$ and, thus, that B_y does not vary inside the boundary layer, whose height is δ, at any given x location. This assumption is difficult to model in a practical multidimensional simulation primarily due to its impact on the boundary layer in the vicinity of the leading edge. In this region, Eq. (29) indicates that the B field is very large and is in fact singular at the leading edge. Coupled with locally high temperatures and, thus, electrical conductivity, the boundary layer separates and invalidates the comparison with semi-analytical results. Simplistic approaches such as setting the B_y field to the value specified by Eq. (29) inside the boundary layer (whose height is determined by velocity, for example), and zero elsewhere also yield unstable numerical solutions. To resolve this difficulty, the B field was obtained separately by solving the magnetic vector potential equation for a flat plate with an imposed field on the surface as described by Eq. (29). Under this condition, the B_y field gradually diminishes away from the plate. To match the body force employed to develop the similarity solution, the conductivity of the fluid inside the boundary layer was enhanced by choosing the T_σ value noted earlier.

The u-velocity profiles, with and without magnetic effects, are plotted in Fig. 4b. For the nonmagnetic case, the method of obtaining compressible boundary-layer similarity profiles degenerates to the classic approach described in Ref. 40. The ordinate is the compressible similarity variable η, whereas the abscissa is $U = u/u_\infty$. For the nonmagnetic case, two different meshes are employed to provide an estimate of adequacy of mesh resolution. Mesh 1 consists of $101 \times 41 \times 5$ points and is highly stretched in the y direction with a minimum spacing of 3.3×10^{-5}. The x-direction spacing is uniform ($\Delta x = 0.01$). Mesh 2 consists of $101 \times 81 \times 5$ points, in which the minimum y-direction spacing is halved to 1.6×10^{-5}. It is evident that the results exhibit mesh independence. The computed results are also in excellent agreement with the semi-analytical results. The velocity profile in the case with the magnetic field has been plotted at two locations spaced 10δ apart, where δ is the height of the boundary layer at the trailing edge of the domain. The overlap of these two profiles indicates that similarity has been achieved. The comparison with theory is similarly excellent in this case. The effect of the magnetic field is seen to yield a significantly shallower velocity profile. Because the surface temperature is identical in both cases and, thus, the molecular viscosity at the wall is also the same, the magnetic field reduces the surface skin-friction coefficient to a substantial extent. In this regard, external flow differs from the Hartmann (internal) flow case explored in Ref. 14, where the impact of the transverse magnetic field is to increase the skin-friction coefficient by yielding a flatter profile near the center of the channel.

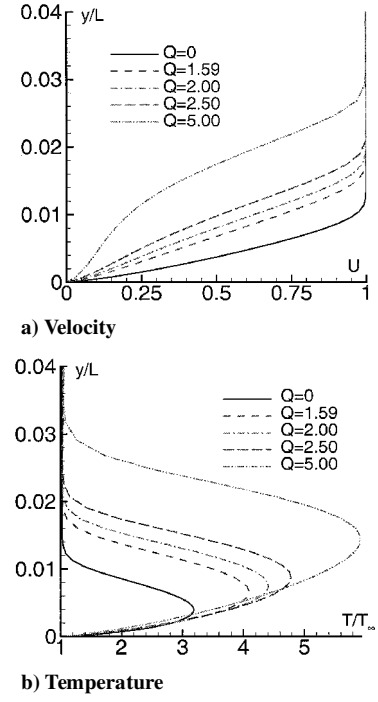

Fig. 5 Effect of interaction parameter Q

This distinction is closely linked to establishment of a specific flow rate in the internal flow situation.

Temperature profiles are shown in Fig. 4c. Again, the nonmagnetic case exhibits not only mesh independence but also excellent agreement with theory. The small discrepancy at the edge of the boundary layer $\eta \sim 13$ is attributable to the existence of a mild leading-edge shock in the computation, which is not modeled in the semi-analytic theory. Modest discrepancies are observed in the case with the magnetic field. In contrast to the velocity profile and despite the high value of the Reynolds number, the temperature profile is observed to be gently varying in the vicinity of the downstream end of the domain. It is not presently clear whether this represents a breakdown of similarity in the temperature profile, perhaps due to the mentioned differences between computational and theoretical problem setup, or whether similarity is recovered farther downstream.

To examine the effect of the magnitude of the magnetic field on the characteristics of the flow, several values of Q are considered in Fig. 5, which shows velocity and temperature profiles at the midpoint of the plate ($Re_x = 2.625 \times 10^5$). The normalized vertical distance from the plate has been chosen as the abscissa to evaluate changes in the height of the boundary layer at this location. In Figs. 5a and 5b, the effect of Q is seen to be monotonic. For all but the largest value of Q plotted, the boundary-layer profile generally resembles that obtained without the magnetic field, but is shallower. This is concomitant with a drop in skin-friction coefficient. Similar observations may be made with respect to the temperature profile. There is far less impact on heat transfer, as measured through the wall temperature gradient, than on skin friction. At $Q = 5.0$, however, the velocity profile exhibits a distinct deficit in momentum, and the temperature gradient at the wall is perceptibly smaller. This is a precursor to boundary-layer separation, and indeed, at even higher values of Q such separation is observed (not shown). Although both skin friction and heat transfer drop sharply as separation is approached, the genesis of this phenomenon is different from the similar effect of increasing Q reported in Ref. 16 because in Ref. 16 separation is not treated.

V. Two-Equation k–ϵ Turbulence Model

The impact of the magnetic field on turbulence is a highly complex phenomenon. Factors include the anisotropy introduced due to the preferential damping of fluctations normal to the field and additional considerations on transition accruing from the generation

of inflection points in velocity profiles.[41] Although a precise analysis would require due consideration of direct numerical simulation techniques, particularly because anisotropy is enhanced by magnetic fields, we focus at present on an engineering approach developed recently for metal flows by Ji and Gardner[21] and modified by Kenjeres and Hanjalic.[20] The method is based on the popular two-equation k–ϵ model, where k is the turbulence kinetic energy and ϵ is its dissipation. The new terms in the model are designed to mimic some of the anticipated effects of the magnetic field in a simple yet effective manner.

Within this philosophy, the impact of the magnetic field can be distinguished by its effect on the mean flow and separately on the fine-scale structure. A simple strategy to model the first phenomenon is to utilize the traditional turbulence model without special modifications. For the second, in Refs. 20 and 21, an additional term is employed for incompressible flows, which is adapted in the present work to treat the compressible case by assuming variable density and introducing a compressibility correction.

The mean flow equations are assumed to be of the same form as discussed earlier in Secs. II and IV with the molecular viscosity μ being replaced by the sum, $\mu + \mu_t$, where μ_t is the eddy viscosity and a turbulent Prandtl number ($Pr_t = 0.9$) is introduced in the standard fashion. The baseline two-equation k–ϵ model including low Reynolds number terms employs the work of several authors.[42–44] In flux vector form and curvilinear coordinates, the governing equations are

$$\frac{\partial \boldsymbol{X}_{k\epsilon}}{\partial t} + \frac{\partial \boldsymbol{F}_{k\epsilon}}{\partial \xi} + \frac{\partial \boldsymbol{G}_{k\epsilon}}{\partial \eta} + \frac{\partial \boldsymbol{H}_{k\epsilon}}{\partial \zeta} = \boldsymbol{S}_{k\epsilon} \tag{30}$$

where

$$\boldsymbol{X}_{k\epsilon} = \frac{1}{J}\begin{bmatrix} \rho k \\ \rho \epsilon \end{bmatrix} \tag{31}$$

and in terms of the contravariant velocities U, V, and W,

$$\boldsymbol{F}_{k\epsilon} = \frac{1}{J}\begin{bmatrix} \rho k U - \left(\mu + \dfrac{\mu_t}{\sigma_k}\right)\xi_{x_i}\dfrac{\partial \xi_j}{\partial x_i}\dfrac{\partial k}{\partial \xi_j} \\ \rho \epsilon U - \left(\mu + \dfrac{\mu_t}{\sigma_\epsilon}\right)\xi_{x_i}\dfrac{\partial \xi_j}{\partial x_i}\dfrac{\partial \epsilon}{\partial \xi_j} \end{bmatrix} \tag{32}$$

where x_i is x, y, or z for $i = 1, 2$, or 3, respectively, and ξ_{x_i}, for example, denotes $\partial \xi / \partial x_i$. Here $\sigma_k = 1$ and $\sigma_\epsilon = 1.3$ are turbulence model constants and are not to be confused with the electrical conductivity σ. Similar expressions may be written for $\boldsymbol{G}_{k\epsilon}$ and $\boldsymbol{H}_{k\epsilon}$. The vector source term is written as

$$\boldsymbol{S}_{k\epsilon} = \frac{1}{J}$$

$$\begin{bmatrix} -\left\{ P_k - \rho\epsilon\left(1 + M_t^2\right) + D - Q\sigma \boldsymbol{B}^2 k \exp\left(-C_1^M Q \dfrac{\sigma}{\rho}\boldsymbol{B}^2 \dfrac{k}{\epsilon}\right)\right\} \\ -\left\{ \dfrac{C_{\epsilon 1} P_k \epsilon}{k} - \dfrac{C_{\epsilon 2} f_{\epsilon 2} \rho \epsilon^2}{k} + E_\epsilon - Q\sigma \boldsymbol{B}^2 \epsilon \exp\left(-C_1^M Q \dfrac{\sigma}{\rho}\boldsymbol{B}^2 \dfrac{k}{\epsilon}\right)\right\} \end{bmatrix} \tag{33}$$

where M_t is the compressibility correction. The last terms in each preceding equation containing Q the interaction parameter, represent the effect of the magnetic field on fine-scale turbulence. The new additional coefficient introduced, C_1^M is taken to be 0.025, although this value was obtained in Ref. 20 for metal flows. Further effort is required to discern the effect of compressibility on this constant, as well as the effect of the magnetic field on the compressibility correction.

The other terms in the preceding equations may be summarized as

$$\mu_t = C_\mu f_\mu Re_t \mu, \qquad Re_t = Re\left(\frac{\rho k^2}{\mu \epsilon}\right), \qquad P_k = \frac{1}{Re}\tau_{t_{ij}}\frac{\partial \xi_k}{\partial x_j}\frac{\partial u_i}{\partial \xi_k}$$

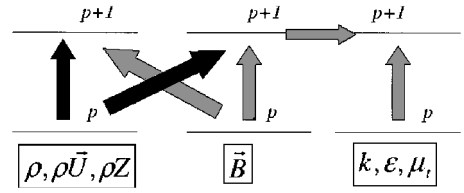

Fig. 6 Schematic of time-integration strategy for k–ϵ equations.

$$\tau_{t_{ij}} = \mu_t\left(\frac{\partial \xi_k}{\partial x_j}\frac{\partial u_i}{\partial \xi_k} + \frac{\partial \xi_k}{\partial x_i}\frac{\partial u_j}{\partial \xi_k} - \frac{2}{3}\delta_{ij}\frac{\partial \xi_l}{\partial x_k}\frac{\partial u_k}{\partial \xi_l}\right), \qquad M_t^2 = \frac{2M_\infty^2 k}{T}$$

$$D = -\frac{2\mu}{Re}\sum_i\left(\frac{\partial \xi_j}{\partial x_i}\frac{\partial k^{\frac{1}{2}}}{\partial \xi_j}\right)^2$$

$$E_\epsilon = \frac{2\mu\mu_t}{\rho Re^2}\sum_i\left(\frac{\partial \xi_k}{\partial x_j}\frac{\partial \xi_l}{\partial x_j}\frac{\partial^2 u_i}{\partial \xi_k \partial \xi_l}\right)^2$$

$$f_\mu = \exp\left[\frac{-3.4}{(1 + 0.02Re_t)^2}\right], \qquad f_{\epsilon 2} = 1 - 0.3\exp\left(-Re_t^2\right)$$

$$C_\mu = 0.09, \qquad C_{\epsilon 1} = 1.44, \qquad C_{\epsilon 2} = 1.92$$

$$\sigma_k = 1.0, \qquad \sigma_\epsilon = 1.3$$

The equations are integrated implicitly in time by extending the loosely coupled procedure described in Sec. III. In this approach, the equation for $\Delta \boldsymbol{X}_{k\epsilon}$ is similar to Eq. (13) except that k, ϵ, and μ_t are lagged, that is, are computed after all components of $\boldsymbol{X}$ have been updated as shown schematically in Fig. 6. This considerably reduces the expense of computing the flux Jacobians. An additional simplification accrues from treating the production terms explicitly, thus, effectively decoupling the k and ϵ equations into two separate scalar equations. For boundary conditions, the values of k, ϵ, and μ_t are all set to zero on walls and standard zero gradient conditions are applied elsewhere.

Several computations have been performed with a view toward exploring features of the turbulence model and its interaction with the mean flow. We consider the nominally two-dimensional flow past a flat-plate boundary layer shown schematically in Fig. 7a. The flow parameters are Mach 4, Reynolds number 3.02×10^5 based on a nominal boundary-layer height of 3.5 mm, freestream temperature T_∞ 63.3 K, and wall temperature fixed at $4.27T_\infty$. Figure 7 tests the implementation of the original k–ϵ model without a magnetic field. The compressibility correction, which is effective in flows with separation and shear layers, was switched off for these cases. The results, in the form of skin-friction coefficient vs Reynolds number based on the local momentum thickness θ, are compared with the semi-empirical formulation of Sommer and Short.[45] Two grids of $121 \times 61 \times 5$ and $201 \times 81 \times 5$ points were employed, uniformly spaced and highly stretched in the x and y directions, respectively. The computations are clearly grid resolved and show excellent agreement with theory. Boundary-layer transition, detected by the sharp rise in skin-friction coefficient, occurs at $Re_\theta \sim 10^3$. The transition location is not specified but arises from the amplification of turbulence from the specified freestream value of 0.005. All subsequent calculations use the $201 \times 81 \times 5$ mesh.

To explore the trends associated with the impact of the magnetic field on turbulence, a two-dimensional dipole is placed at a distance of 55δ downstream of the leading edge and 0.1δ beneath the plate (Fig. 7a). The more practical exercise of stringing several dipoles sequentially was not explored in this work. The magnetic field due to the dipole is given by

$$\begin{Bmatrix} B_x \\ B_y \\ B_z \end{Bmatrix} = \frac{1}{(x^2 + y^2)^2}\begin{Bmatrix} 4xy \\ 2(x^2 - y^2) \\ 0 \end{Bmatrix} \tag{34}$$

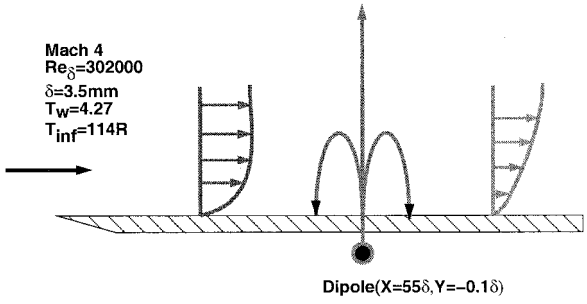

a) Schematic

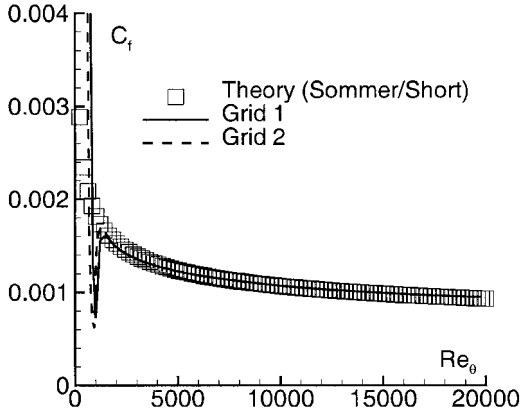

b) Skin-friction coefficient without magnetic field

Fig. 7 Turbulent flow past flat plate: implementation of baseline model.

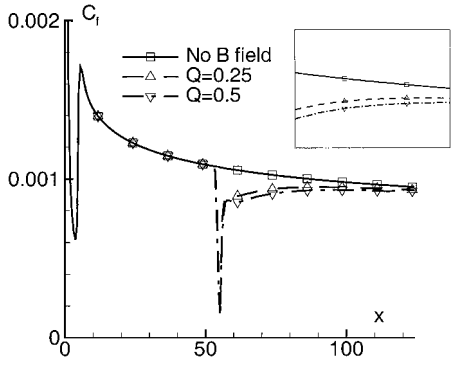

Fig. 8 Effect of magnetic field on C_f.

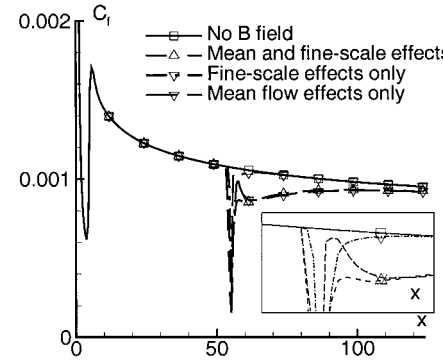

a) Skin-friction coefficient

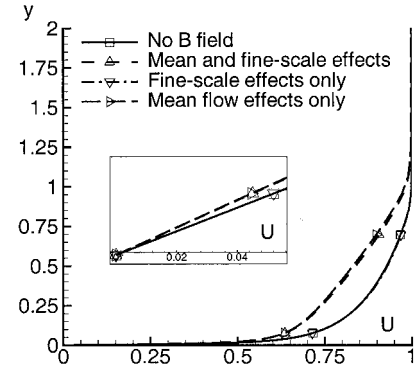

b) Velocity profile

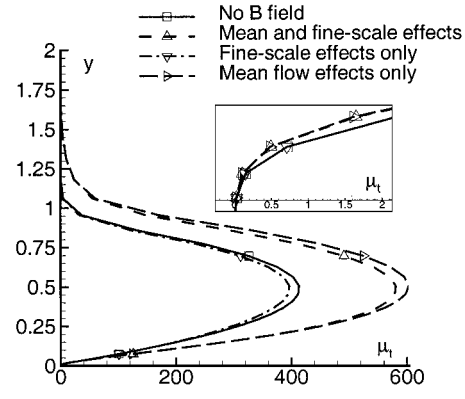

c) Eddy viscosity

Fig. 9 Impact of magnetic field on the mean flow and fine-scale turbulence.

where x and y are the distance to each grid point from the dipole origin. The magnetic field is scaled to yield a maximum magnitude of unity in the domain of computation and is assumed to be unperturbed under the low-magnetic-Reynolds-number Re_σ approximation.

Figure 8 shows the impact of the dipole on the skin-friction coefficient at two different values of the interaction parameter $Q = 0.25$ and 0.50. The abscissa is the streamwise distance x normalized by the nominal boundary-layer thickness. For convenience, the electrical conductivity is assumed to vary as $\sigma^* = (T^* - 1)^{3/2}$ so that the far field is nonconducting. With reference to Fig. 8, the skin-friction coefficient shows a decline in the vicinity of the dipole but shows a gradual recovery near the trailing edge. The effect of Q is principally observed downstream of the initial drop, where C_f recovery is marginally faster at the smaller interaction parameter. Analysis of the flowfield (not shown) reveals the development of a weak shock upstream of the dipole, consistent with the displacement effect of the retarding Lorentz force.

To further explore the relative importance of the interaction between the magnetic field with the mean flow on the one hand and with the fine-scale quantities on the other, the case with $Q = 0.5$ was run first without the extra terms in Eq. (33) but with the source term S of Eq. (27) on and, subsequently, with the reverse situation where the magnetic field affects only the k and ϵ equations but not the mean flow directly. The results are shown in Fig. 9, which shows the effect on the skin-friction coefficient and on velocity and eddy viscosity profiles 15δ downstream of the dipole. It is evident that in the context of the present model the dominant effect of the magnetic field is on the interaction with the mean flow. The velocity profile shows the thickening of the boundary layer and the corresponding reduction in velocity gradient at the surface. The eddy viscosity (Fig. 9c) shows the interesting feature that the peak values of μ_t actually increase from about 400μ without the magnetic field to about 600μ (again, principally due to the direct impact of the Lorentz force on the mean flow). In this region velocity gradients are not large and stresses due to the eddy viscosity are correspondingly small. However, as the inset in Fig. 9 shows, in all cases, the eddy viscosity is diminished in the critically important near-wall region comprising the viscous sublayer, where the velocity gradient and the impact of viscous stresses are large.

A comparison of the effect of the magnetic field on laminar and turbulent boundary layers is presented in Fig. 10 at $Q = 0.5$ in

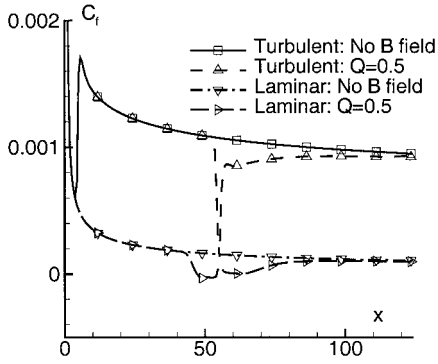

a) Skin-friction coefficient

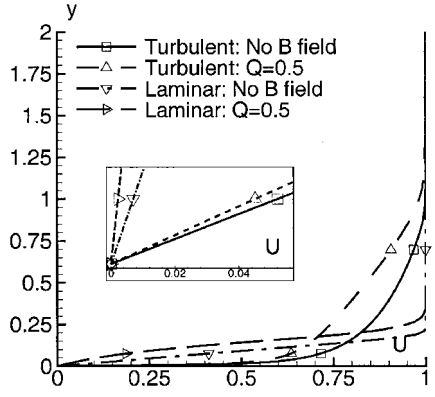

b) Velocity profile

Fig. 10 Comparison of effect of magnetic field on laminar and turbulent flow.

respect to C_f and u velocity at 15δ from the location of the dipole. Without the magnetic field, C_f values are much smaller in laminar flow as expected. The surface velocity gradient is correspondingly smaller, and the boundary layer is much thinner. The magnetic field increases the height of the boundary layer in both cases and reduces surface gradients. The upstream influence of the dipole is much larger in the laminar case, consistent with the larger subsonic region, and the skin-friction coefficient changes more gradually. However, the effect of the magnetic field persists for a longer distance in the turbulent flow.

VI. Exploratory Simulation of MGD Reentry Vehicle Flow Control

To highlight issues related to the simulation of MGD control of external flow past a geometrically complex configuration, the last case considers flow past the X24C reentry vehicle (Fig. 11a). The X24C exhibits several generic characteristics of modern high-speed aerospace vehicle designs. The configuration was proposed as an air-launched, rocket-powered configuration to serve as a test bed for experimental programs at or exceeding Mach 6. This geometrical complexity results in a flow with a variety of interacting features: boundary layers, shock waves, expansion fans, and vortical flow. The flowfield (without MGD control) past this craft has been examined in an earlier effort,[46] and a wealth of data are available from turbulent wind-tunnel experiments for validation.[47] The flow parameters are chosen to match those employed in earlier efforts and consist of a Mach number of 5.95 and a Reynolds number of 1.5×10^6/m, where the wall is assumed to be adiabatic. The magnetic Reynolds number is assumed to be small enough to invoke the low-magnetic-Reynolds-number Re_σ approximation. Van Leer's scheme is employed together with the other elements listed in Sec. IV. The conductivity is assumed to scale with the temperature in the manner of Eq. (28), and to obtain significant MGD interaction, n is set to 4.1.

The coordinate system is positioned so that the x axis is aligned with the oncoming flow, the z axis is oriented spanwise, and the y axis points in the vertical direction. To explore MGD flow control, four dipoles are placed inside the body, in the vicinity of regions where fluid dynamic load is expected to be high, namely, at the nose and at the bases of the vertical and middle fins. Each dipole is scaled in such a manner that the magnetic field at the nearest point on the body surface is unity. The magnitude of the surface magnetic field, which at any spatial point is the vector sum of the contribution due to each dipole, is shown in Fig. 11a. The axes of all dipoles are aligned with the streamwise, x direction. Figure 11b shows selected field lines due to the dipole at the nose. Because the resulting configuration is symmetric, and the Hall effect has been neglected, the flow is computed only on one side of the vertical plane of symmetry. The nominal mesh consists of $128 \times 36 \times 110$ points, which is sufficient to define the surface geometry and to discern principal aspects of the flowfield when high-resolution schemes are employed. (In Ref. 46, a grid resolution study for the no-MGD case is presented.)

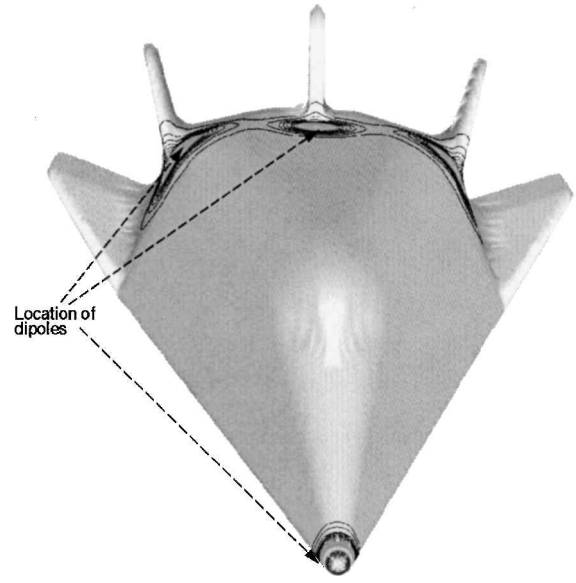

a) Location of magnetic dipoles

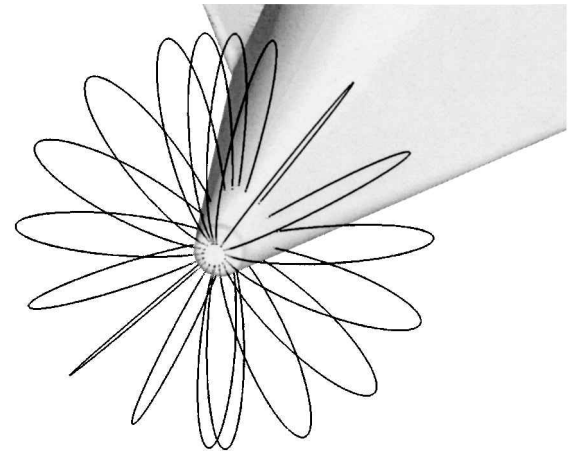

b) Selected magnetic field lines of dipole at nose

Fig. 11 X24C reentry vehicle.

Figures 12a–12c show the surface pressure, wall temperature, and skin-friction coefficient, without (left-hand side) and with (right-hand side) the magnetic field at a value of $Q = 1.0$. Two conclusions are readily apparent. First, despite the fact that all dipoles are of approximately the same magnitude, those near the nose and in the vicinity of the middle fin have significant impact on the flow, whereas that located near the vertical fin has negligible influence. This follows from the expectation that the relative orientation of the flow and magnetic field is important in exerting control. However,

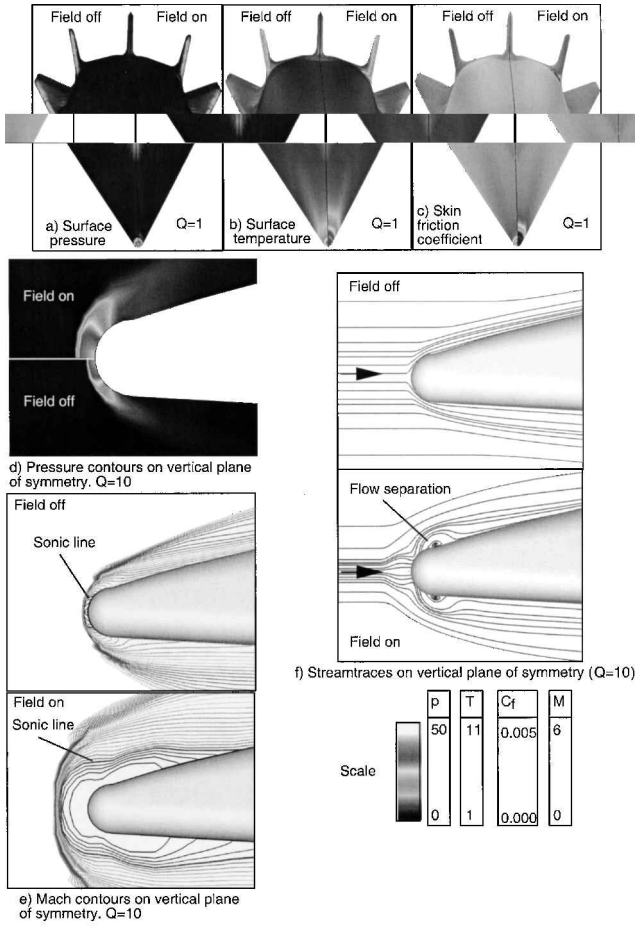

Fig. 12 Various aspects of impact of magnetic field on flow past reentry vehicle: p and T are normalized by their freestream values.

surface pressure shows a small increase (5% at the stagnation point) rather than a reduction anticipated from theory,[48] which suggests that the effect of placing a dipole at the center of a hemispherical body such as at the nose of the vehicle should diminish this quantity substantially. Moreover, surface temperature rises by over 10%. Evidently, in this case, the magnetic field has actually enhanced surface load. Only the skin-friction coefficient falls to near-zero values near the nose but recovers rapidly downstream of the nose.

This behavior is examined in greater detail by raising the magnetic field intensity so that $Q = 10$. Figure 12d shows pressure on the vertical plane of symmetry for this case. The shock standoff distance increases due to the presence of the field. This is consistent with theoretical results[48] and experimental observations[3] of blunt-body flows in the presence of magnetic fields. However, for reasons noted later, complete characterization requires additional fluid dynamic considerations because pressure recovery downstream of the shock is much higher (by 9%) and is not consistent with results from the literature. Mach number contours (Fig. 12e) also show an increase in shock standoff distance, but the region of subsonic flow has increased substantially extending well beyond the nose. In contrast, when the magnetic field is absent, the sonic line enters the boundary layer in the hemisphere-nose part of the forebody. To investigate the flowfield further, Fig. 12f show particle traces on the vertical plane of symmetry. Whereas the flow is attached when the magnetic field is off, it separates downstream of the nose when the magnetic field is on. The inception of flow separation can be due to complicated fluid dynamic factors, and in the present case, the choice of conductivity profile and neglect of induced electric fields introduces an additional element of uncertainty. A possible mechanism for the preceding observation may be proposed, based on the flat-plate results of Sec. III, that magnetic fields act to reduce shear stress and indeed, by themselves, can induce separation of the momentum deficient flow inside the boundary layer. In the case of the reentry vehicle, separation alters the entire dynamics of the flow past the forebody because of the large extent of the subsonic domain. This example suggests a possible difficulty that may be encountered in the use of magnetic forces. Flow control with beneficial effects in one region may have adverse reaction elsewhere, particularly because, in many respects, magnetic forces exhibit the action at a distance property.

VII. Conclusions

An efficient and accurate procedure is presented to facilitate the numerical simulation of potentially revolutionary three-dimensional hypersonic flow control techniques. A loosely coupled, second-order, subiterative, implicit-time integration method based on approximate factorization is shown to alleviate the stability constraints of explicit schemes on the highly stretched meshes required to resolve flows of practical importance in magnetoaerodynamics. The basic phenomena of wave propagation and diffusion are simulated to quantify the benefits of the time-integration method. Computations of flat-plate boundary-layer flows with imposed magnetic fields verify the low-magnetic-Reynolds-number formulation and show that magnetic fields can reduce skin-friction coefficient. Because most flows of interest are likely to be turbulent, a two-equation compressible k–ϵ model with low-Reynolds-number terms to treat wall-bounded flows is incorporated into the simulation method. For the case of a dipole placed under a turbulent flat-plate boundary layer at Mach 4, the primary effects are seen to arise from the interaction of the magnetic field directly with the mean flow and additional terms in the turbulence model play a secondary role. Differences between the responses of magnetic fields on laminar and turbulent flows are summarized. An exploratory study of control of a reentry vehicle shows that the implicit technique can provide solutions on complex configurations. Conclusions regarding MGD control, derived from the several problems considered, are predicated on choices made to facilitate comparison with available analytic or experimental data or for numerical convenience. The results suggest that MGD can be fruitfully utilized to exert beneficial control of high-speed flow, but that a careful examination of all aspects of magnetic field interaction must be conducted to avoid unintended consequences.

Acknowledgments

The authors are grateful for Air Force Office of Scientific Research sponsorship under tasks monitored by W. Hilbun and J. Schmisseur and by a grant of computer time from the Department of Defense High Performance Computing Shared Resource Centers at the Aeronautical Sciences Center, the Army Engineer Research and Development Center, and the Naval Oceanographic Office. The authors have also benefited from the comments and suggestions of several researchers, including R. MacCormack, S. Macheret, U. Mehta, C. Park, J. Shang, M. Visbal, and J. Young.

References

[1]Shang, J. S., Hayes, J., and Menart, J., "Hypersonic Flow over a Blunt Body with Plasma Injection," AIAA Paper 2001-0344, Jan. 2001.

[2]Riggins, D. W., and Nelson, H. F., "Hypersonic Flow Control Using Upstream Focused Energy Deposition," *AIAA Journal*, Vol. 38, No. 4, 2000, pp. 723–725.

[3]Ziemer, R. W., and Bush, W. B., "Magnetic Field Effects on Bow Shock Stand-off Distance," *Physical Review Letters*, Vol. 1, No. 2, 1958, pp. 58, 59.

[4]Gurijanov, E. P., and Harsha, P. T., "AJAX: New Directions in Hypersonic Technology," AIAA Paper 96-4609, Nov. 1996.

[5]Shang, J. S., Hayes, J., Menart, J., and Miller, J., "Blunt Body in Hypersonic Electromagnetic Flow Field," AIAA Paper 2001-2803, June 2001.

[6]Kuranov, A. L., Kuchinsky, V. V., and Sheikin, E. G., "Scramjet with MHD Control Under 'AJAX' Concept. Requirements for MHD Systems," AIAA Paper 2001-2881, June 2001.

[7]Park, C., Bogdanoff, D. W., and Mehta, U. B., "Theoretical Performance of a Nonequilibrium MHD-Bypass Scramjet," AIAA Paper 2001-0792, Jan. 2001.

[8]Macheret, S. O., Shneider, M. N., and Miles, R. B., "Electron-Beam-Generated Plasmas in Hypersonic Magnetohydrodynamic Channels," *AIAA Journal*, Vol. 39, No. 6, 2001, pp. 1127–1138.

[9]Barmin, A. A., Kulikovskiy, A. G., and Pogorelov, N. V., "Shock-Capturing Approach and Nonevolutionary Solutions in Magnetohydrodynamics," *Journal of Computational Physics*, Vol. 126, No. 1, 1996, pp. 77–90.

[10]Rosa, R. J., *Magnetohydrodynamic Energy Conversion*, McGraw–Hill, New York, 1968, Chap. 3.

[11]Damevin, H.-M., Dietiker, J.-F., and Hoffmann, K. A., "Hypersonic Flow Computations with Magnetic Field," AIAA Paper 2000-0451, Jan. 2000.

[12]MacCormack, R. W., "An Upwind Conservation Form Method for the Ideal Magneto-Hydrodynamics Equations," AIAA Paper 99-3609, June 1999.

[13]MacCormack, R. W., "A Computational Method for Magneto-Fluid Dynamics," AIAA Paper 2001-2735, June 2001.

[14]Gaitonde, D. V., "Higher-Order Solution Procedure for Three-Dimensional Nonideal Magnetogasdynamics," *AIAA Journal*, Vol. 39, No. 1, 2001, pp. 2111–2120.

[15]Beam, R., and Warming, R., "Implicit Factored Scheme for the Compressible Navier–Stokes Equations," *AIAA Journal*, Vol. 16, No. 4, 1978, pp. 393–402.

[16]Bush, W. B., "Compressible Flat-Plate Boundary-Layer Flow with an Applied Magnetic Field," *Journal of the Aero/Space Sciences*, Vol. 27, No. 1, 1960, pp. 49–58.

[17]Shercliff, J. A., *A Textbook of Magnetohydrodynamics*, Pergamon, Oxford, 1965, Chap. 4.

[18]Gaitonde, D. V., and Poggie, J., "An Implicit Technique for 3-D Turbulent MGD with the Generalized Ohm's Law," AIAA Paper 2001-2736, June 2001.

[19]Dietiker J.-F., and Hoffmann, K. A., "Numerical Simulation of Turbulent Magnetohydrodynamic Flows," AIAA Paper 2001-2737, June 2001.

[20]Kenjeres, S., and Hanjalic, K., "On the Implementation of Effects of Lorentz Force in Turbulence Closure Model," *International Journal of Heat and Fluid Flow*, Vol. 21, No. 3, 2000, pp. 329–337.

[21]Ji, H.-C., and Gardner, R. A., "Numerical Analysis of Turbulent Pipe Flow in a Transverse Magnetic Field," *International Journal of Heat and Mass Transfer*, Vol. 40, No. 8, 1997, pp. 1839–1851.

[22]Anderson, D. A., Tannehill, J. C., and Pletcher, R. H., *Computational Fluid Mechanics and Heat Transfer*, McGraw–Hill, New York, 1984, Chap. 5.

[23]Lele, S. K., "Compact Finite Difference Schemes with Spectral-Like Resolution," *Journal of Computational Physics*, Vol. 103, No. 1, 1992, pp. 16–42.

[24]Gaitonde, D. V., Shang, J. S., and Young, J. L., "Practical Aspects of Higher-Order Numerical Schemes for Wave Propagation Phenomena," *International Journal for Numerical Methods in Engineering*, Vol. 45, 1999, pp. 1849–1869.

[25]Visbal, M., and Gaitonde, D. V., "Very High-Order Spatially Implicit Schemes for Computational Acoustics on Curvilinear Meshes," *Journal of Computational Acoustics*, Vol. 9, No. 4, 2001, pp. 1259–1286.

[26]Jameson, A., Schmidt, W., and Turkel, E., "Numerical Solutions of the Euler Equations by a Finite Volume Method Using Runge–Kutta Time Stepping Schemes," AIAA Paper 81-1259, July 1981.

[27]Gaitonde, D. V., "Development of a Solver for 3-D Non-ideal Magnetogasdynamics," AIAA Paper 99-3610, June 1999.

[28]Gaitonde, D. V., and Poggie, J., "Simulation of Magnetogasdynamic Flow Control Techniques," AIAA Paper 2000-2326, June 2000.

[29]Conte, S. D., and de Boor, C., *Elementary Numerical Analysis—An Algorithmic Approach*, McGraw-Hill, New York, 1980, Chap. 8.

[30]Warming, R. F., and Beam, R. M., "Upwind Second-Order Difference Schemes and Applications in Aerodynamic Flows," *AIAA Journal*, Vol. 14, No. 9, 1976, pp. 1241–1249.

[31]Visbal, M. R., and Gaitonde, D. V., "High-Order Accurate Methods for Unsteady Vortical Flows on Curvilinear Meshes," AIAA Paper 98-0131, Jan. 1998.

[32]Powell, K. G., "An Approximate Riemann Solver for Magnetohydrodynamics," ICASE Rept. 94-24, NASA Langley Research Center, 1994.

[33]Pulliam, T. H., and Steger, J. L., "Implicit Finite-Difference Simulation of Three-Dimensional Compressible Flow," *AIAA Journal*, Vol. 18, No. 2, 1980, pp. 159–167.

[34]Brio, M., and C. C., Wu, "An Upwind Differencing Scheme for the Equations of Ideal Magnetohydrodynamics," *Journal of Computational Physics*, Vol. 75, No. 2, 1988, pp. 400–422.

[35]Hughes, W. F., and Young, F. J., *The Electromagnetodynamics of Fluids*, Wiley, New York, 1966, Chap. 2.

[36]Gaitonde, D. V., and Poggie, J., "Elements of a Numerical Procedure for 3-D MGD Flow Control Analysis," AIAA Paper 2002-0198, Jan. 2002.

[37]Roe, P. L., "Approximate Riemann Solvers, Parameter Vectors and Difference Schemes," *Journal of Computational Physics*, Vol. 43, No. 2, 1981, pp. 357–372.

[38]van Leer, B., "Flux-Vector Splitting for the Euler Equations," ICASE Rept. 82-30, NASA Langley Research Cener, Sept. 1982.

[39]van Leer, B., "Towards the Ultimate Conservation Difference Scheme V, A Second-Order Sequel to Godunov's Method," *Journal of Computational Physics*, Vol. 32, No. 1, 1979, pp. 101–136.

[40]White, F. M., *Viscous Fluid Flow*, McGraw–Hill, New York, 1991, Chap. 7.

[41]Sato, H., "The Hall Effect in the Viscous Flow of Ionized Gas Between Parallel Plates Under Transverse Magnetic Field," *Journal of the Physical Society of Japan*, Vol. 16, No. 7, 1961, pp. 1427–1433.

[42]Launder, B. E., and Sharma, B. I., "Application of the Energy Dissipation Model of Turbulence to the Calculation of Flows near a Spinning Disk," *Letters in Heat and Mass Transfer*, Vol. 1, No. 1, 1974, pp. 131–138.

[43]Sarkar, S., Erlebacher, G., Hussaini, M. Y., and Kreiss, H. O., "The Analysis and Modelling of Dilational Terms in Compressible Turbulence," *Journal of Fluid Mechanics*, Vol. 227, 1991, pp. 473–493.

[44]Rizzetta, D. P., "Numerical Simulation of Vortex-Induced Oblique Shock-Wave Distortion," *AIAA Journal*, Vol. 35, No. 1, 1997, pp. 209–211.

[45]Sommer, S. C., and Short, B. J., "Free-Flight Measurements of Turbulent Boundary-Layer Skin Friction in the Presence of Severe Aerodynamic Heating at Mach Numbers from 2.8 to 7.0," *Journal of the Aeronautical Sciences*, Vol. 23, No. 6, 1956, pp. 536–542.

[46]Gaitonde, D. V., and Shang, J. S., "Numerical Simulation of Flow past the X24C Reentry Vehicle," AIAA Paper 93-0319, Jan. 1993.

[47]Wannernwetsch, G. D., "Pressure Tests of the AFFDL X-24C-10D Model at Mach Numbers of 1.5, 3.0, 5.0 and 6.0," von Kármán Gas Dynamics Facility, TR AEDC-DR-76-92, Arnold Engineering Development Center, Arnold AFB, TN, 1976.

[48]Bush, W. B., "Magnetohydrodynamic-Hypersonic Flow past a Blunt Body," *Journal of the Aero/Space Sciences*, Vol. 25, No. 11, 1958, pp. 685–690, 728.

P. Givi
Associate Editor